

SOLAR ECLIPSE-INDUCED PERTURBATIONS AT MID-LATITUDE DURING THE 21 AUGUST 2017 EVENT

Bolarinwa J. Adekoya¹, Babatunde O. Adebisin², Timothy W. David¹, Stephen O. Ikubanni², and
Shola J. Adebisi²

¹Department of Physics, Olabisi Onabanjo University, P.M.B. 2002, Ago Iwoye, Nigeria

²Space Weather Group, Department of Physical Sciences, Landmark University, P.M.B 1001, Omu-Aran,
Kwara State, Nigeria.

Correspondence to: Bolarinwa J. Adekoya (adekoyabolrinwa@yahoo.com; adekoya.bolarinwa@oouagoiwoye.edu.ng)

Abstract

A study of the response of some ionospheric parameters and their relationship in describing the behaviour of ionospheric mechanisms during the solar eclipse of 21 August 2017 is presented. Mid-latitude stations located along the eclipse path and with data availability on the Global Ionospheric radio Observatory (GIRO) database were selected. The percentage of obscuration at these stations range between 63-100%. Decrease in electron density during the eclipse is attributed to reduction in solar radiation and natural gas heating. The maximum magnitude of the eclipse coincided with $hmF2$ increase and with a lagged maximum decrease in $NmF2$ consistently at the stations investigated. The results revealed that the horizontal neutral wind flow is as a consequence of the changes in the thermospheric and diffusion processes. The unusual increase/decrease in the shape/thickness parameters during the eclipse period relative to the control days points to the perturbation caused by the solar eclipse. The relationship of the bottomside ionosphere and the F2 layer parameters with respect to the scale height are shown in the present work as viable parameters for probing the topside ionosphere during eclipse. Furthermore, this study shows that in addition to traditional ways of analysing the thermospheric composition and neutral wind flow, proper relation of standardized $NmF2$ and $hmF2$ can be conveniently used to describe the mechanisms.

Keywords: solar eclipse; solar radiation; bottomside profile parameters; $NmF2$ and $hmF2$; Topside ionosphere; GIRO database.

1 Introduction

Solar eclipse provides opportunity to study the causes of drastic changes in the atmosphere arising from reduction in solar radiation and plasma flux. The atmosphere responded to these changes by modifying the electrodynamic processes and ionization supply of its species to the nighttime-like characteristics during the daytime. Different physical mechanisms (e.g. neutral wind, thermospheric composition, diffusion process etc.) that explain the distribution of plasma at the different ionospheric layers are well established.

38 However, these mechanisms do compete with themselves in explaining the ionosphere, especially the
39 topside ionosphere (see Gulyaeva, 2011).

40

41 At mid-latitudes, the effect of diffusion processes and its relationship with the thermospheric compositions
42 has been extensively studied during episodes of solar eclipse (Muller-Wodarg et al., 1998; Jakowski et al.,
43 2008; Le et al., 2009; Wang et al., 2010; Chuo, 2013). At equatorial and low-latitude regions, the $E \times B$
44 plasma drift had been used to explain the circumstances of solar eclipse on transport processes (Adeniyi et
45 al., 2007; Adekoya et al., 2015). Recently, attention has been drawn to the study of the topside ionosphere
46 during an eclipse for improved prediction and modelling (Huba and Drob, 2017; Chrniak and Zakharenkova,
47 2018). Reinisch et al., (2018) compared the modelled and measured studies of electron densities at the
48 altitude range of about 150 - 400 km during the eclipse. They found that at lower altitude (at about 150 km)
49 the modelled and the measured agreed well to the changes in the altitude profile of electron density
50 compared to at higher altitudes. The authors however posited that it would be improved if the model
51 $NmF2$ peak falls more slowly to better match the data. Consequently, the present study investigates the
52 effects of solar eclipse of August 21, 2017 on the constituents of the ionosphere at mid-latitudes using
53 some ionosonde data (bottomside parameters, scale height (H) estimated from the fitted α -Chapman layer)
54 which have not been given much attention in previous works especially in analysing solar eclipse effect.
55 Using these parameters to analyse the circumstances of solar eclipse at the topside ionosphere and its
56 plasma distribution mechanisms make this paper significantly different from previous studies. This, we
57 intend to achieve by analysing the ionospheric parameters that controls the distribution of plasma at the
58 topside and bottomside layers of the F2 region. To shed light on these analysis, section 2 highlights the data
59 source, methodology, and path of the eclipse. The result and discussion were presented in section 3, while
60 section 4 presents the summary and concluding remark of the result.

61

62 **2 Data source, methodology, and the path of the eclipse**

63 With regards to the eclipse of 21 August 2017, the totality of the eclipse is visible from within a narrow
64 corridor that traverses the United States of America. However, in the surrounding areas, which include all
65 of mainland United States and Canada, the eclipse was partial. More details of its path can be seen via
66 NASA – Total solar eclipse of 2017 August 21 (<https://eclipse.gsfc.nasa.gov/>). From the footprint of the
67 Moon's shadow as seen from some locations, the eclipse started from around 08:00 LT and ended around
68 14:30 LT (not shown). The details on the local circumstances of the eclipse, the time of the first, mid and
69 last contact of the eclipse over the ionosphere of the investigated stations were highlighted in table 1.
70 More details on the total solar eclipse event and its partiality, the circumstances surrounding its
71 progression and its magnitude of obscuration can be obtained through the link

72 http://xjubier.free.fr/en/index_en.html. The ionospheric parameters data used for this study for the
73 selected mid-latitude stations were obtained from the Global Ionospheric Radio Observatory (GIRO)
74 networks (Reinisch and Galkin 2011) and manually validated. The parameters include the maximum
75 electron density of the F2-layer ($NmF2$, m^{-3}), and its height ($hmF2$, km), the shape parameter ($B1$), the
76 thickness parameter ($B0$), and the Chapman scale height (H) of the F2 layer. The path of the eclipse
77 informed the choice of stations.

78 $NmF2$ values for both the eclipse and control days were obtained from their corresponding critical
79 frequencies ($foF2$) using the expression: $NmF2 = ((foF2)^2 / 80.5) e/m^3$. The control day value is the average
80 value of the two days before/after the eclipse day (i.e. 6, 12, 24 and 27). These reference days were chosen
81 such that they have similar geomagnetic, interplanetary and solar properties with the eclipse day. The daily
82 average value of control days and eclipse day interplanetary index (Ap and ΣKp), and solar flux unit index
83 ($F10.7$) ranges from 8 – 12 nT for Ap , 20 – 27 nT for ΣKp and 75.6 – 89.1 sfu (1 solar flux unit (sfu) = 10^{-22}
84 $Wm^{-2} Hz^{-1}$) for $F10.7$, indicating that geomagnetic and solar activities of these days is unsettled (see
85 Adekoya et al., 2015 for classification of geomagnetic activity). The calculated daily average of summation
86 Kp , Ap and solar flux indices was obtained from the National Space Science data Centres (NSSDC's) OMNI
87 database <https://omniweb.gsfc.nasa.gov/>. The typical behaviour of the $NmF2$ and $hmF2$ on the eclipse day
88 (i.e. $NmF2e$ and $hmF2e$) was compared with that of the control day ($NmF2c$ and $hmF2c$) to observe the
89 changes brought by the short period of loss of photoionization in the ionosphere. This will measure the
90 direct consequence of the solar radiation disruption (due to the eclipse) on the ionospheric chemical,
91 transport and thermal processes in the F2 layer. The ionized layer depends majorly on three parameters,
92 viz: $NmF2$, $hmF2$, and the ionospheric scale height (H). The H describes the constituents of the ionospheric
93 plasma, which decreases with increasing altitude. It is estimated from the fitted α -Chapman layer with a
94 variable scale height, $H(h)$, to the measured bottomside profile $N(h)$, which then determined as the
95 Chapman scale height at $hmF2$ (i.e. $H(hmF2) = H$) (Huang and Reinisch 2001; Reinisch and Huang 2001).
96 Together with the information of $NmF2$ and $hmF2$, the topside profile can be best represented, which is
97 assumed to follow the α -Chapman function (Huang and Reinisch 2001). Also, H provides a linkage between
98 the bottomside ionosphere and the topside profiles of the F region (Liu et al., 2007).

99

100 However, Xu et al. (2013) and Gulyaeva (2011) related ionospheric F2 - layer scale height, H to the topside
101 base scale height, Hsc , given by $Hsc = hsc - hmF2 \approx 3 \times H$. Where hsc is the height at which the electron
102 density of the F2-layer falls by a factor of an exponent, at an upper limit of 400 km altitude (i.e. $NmF2/e$)
103 (see Xu et al., 2013). That is, the region where electron density profile gradient is relatively low. Gulyaeva
104 (2011) showed theoretically that Hsc increase over Hm by a factor of approximately three (3) and is a

105 consequence of the $Ne/NmF2$ ratio (Ne – plasma density), which corresponds to H in the Chapman layer. At
106 altitudes very close to $hmF2$, the ratio equals 0.832, while it is 0.368 at altitudes beyond the $hmF2$.
107 Therefore, we adopted the definition of Gulyaeva (2011) for the topside base scale height as the region of
108 the ionosphere between the F2-peak and 400 km altitude. Summarily, the topside based scale height
109 ionosphere here is defined as the region between the F2 peak and hsc or $3H$. It is thus evident that H is a
110 key and essential parameter in the continuity equation for deriving the production rate at different
111 altitudes, a pointer to the F2 topside electron profiler, as well as a good parameter for evaluating the
112 transport term (Yonezawa, 1966; Huang and Reinisch, 2001; Reinisch and Huang, 2001; Belehaki et al.,
113 2006; Reinisch et al., 2004). Consequently, the parameter H can be used as a proxy for observation relating
114 to the topmost side electron density profile. Furthermore, the division of the topsides and the bottomside
115 ionosphere may be related to the difference in the effective physical mechanisms in the regions. Hence, the
116 bottomside parameters $B1$ and $B0$ of the ionosphere, as presented in this work, helped in examining the
117 perturbation of solar eclipse in the bottomside ionospheric F2 layer.

118

119 **3 Result and Discussion**

120 This section presents the temporal evolution of the maximum electron density ($NmF2$), and its
121 corresponding height ($hmF2$) over the ionosphere at the selected mid-latitude stations along the path of
122 solar eclipse of 21 August 2017. The control day variation relative to the eclipse day is also presented.
123 Figure 1 presents the variation of maximum electron density and the corresponding peak height, during
124 both the eclipse and control days. Figure 2 depicts the variation of scale height and the bottomside
125 parameters ($B0$ and $B1$) due to the eclipse by superposing plots for both the eclipse and control days.
126 Analysis of these parameters during an eclipse event may help in the modelling of the ionospheric profiles
127 (the topsides and bottomside electron density distribution profile) during the short nighttime-like period of
128 the day. Figure 1a presents the $NmF2$ and $hmF2$ variations during the eclipse event and the control day
129 over Austin; having an obscuration magnitude of 65.93% around the daytime period. The effect of the
130 disruption of solar radiation was evident as the $NmF2$ started decreasing at the first contact of the eclipse
131 in Fig. 1ai. The start time or first contact, the maximum magnitude period and the end time or the last
132 contact of the eclipse are marked with the vertical lines S, M and E respectively. The decrement in $NmF2$
133 during the eclipse phase was due to reduction in the ionization. This reduction caused changes in the
134 photochemical and transport process of the atmosphere during the daytime, thus exhibiting nighttime
135 characteristics. It should be noted that the maximum decrease in $NmF2$ did not coincide with the maximum
136 magnitude of the eclipse obscuration, rather with a time lag of few minutes. This lag period fell within the
137 relaxation period over Austin ionosphere, with $NmF2$ and $hmF2$ simultaneously attaining their peak

138 magnitudes. Hence, the ionosphere returned to its pre-eclipse state. Contrary to the decrease in the *NmF2*
139 amplitude, the *hmF2* increased at the total obscuration of the eclipse window.

140

141 The ionosphere over Eglin AFB, Boulder, Point Arguello, Millstone Hill and Idaho National Lab, did not show
142 any contrary variation to that observed at Austin during the eclipse event. The decrease and increase in
143 *NmF2* and *hmF2* after the maximum magnitude was simultaneous. The only exception was that the local
144 time at which each station observed the effects were different. Their obscuration percentage ranged from
145 62.5 – 100%. This did not cause any significant change in the way they responded to the reduction in solar
146 heating. The ionosphere over Idaho National Lab experienced the totality of the eclipse with 100 %
147 magnitude, the *hmF2* was observed to increase few minutes before the maximum magnitude of the
148 obscuration. However, other stations responded differently, their *hmF2* peak enhancement was observed
149 after the maximum obscuration. All these observations may be linked with the fact that the level of
150 minimum rate of electron production does not necessarily coincide with peak electron density of the
151 molecular gases formed. This is because the electron concentration depends on the loss rate by dissociative
152 recombination too.

153

154 At mid-latitudes, the ionospheric F2 plasma distribution is controlled by diffusion processes (Rishbeth
155 1968). There are two basic mechanisms that define the diffusion process during an eclipse: First is the
156 coolness brought by the partial removal of photoionization (Müller-Wodarg et al., 1998), which is believed
157 to be the originator of the downward diffusion process, and the atmospheric expansion due to the gradual
158 increase in the temperature after the totality. The downward diffusion process was related to the increase
159 in the molecular gas (N_2) concentration during the cooling process. However, the aftermath of the coolness
160 was related to the upward diffusion process. These mechanisms were proxy to the electron density
161 distribution during the eclipse window. Our analysis suggests that the observed decrease in *NmF2* is due to
162 the downward diffusion flux of the plasma while the increase that followed is by upward diffusion (e.g. Le
163 et al., 2009; Adekoya and Chukwuma 2016). Several works on eclipse (Müller-Wodarg et al., 1998;
164 Grigorenko et al., 2008; Adekoya and Chukwuma 2016; Hoque et al., 2016) have shown that it was not just
165 the electron density that is being affected during an eclipse window, but the thermospheric wind as well,
166 since the thermospheric wind emanating from the ratio of gas species is related to the variation in electron
167 density. It has been observed that the increase in the mean molecular gas of thermospheric composition
168 decreases the electron density and vice versa. Le et al. (2010) related the trough of electron density
169 distribution during the eclipse phases to the contraction/compression and expansion of the atmosphere
170 brought by the decrease and increase in temperature; leading to the downward drift of the plasma during
171 the eclipse window. Chukwuma and Adekoya (2016) attributed the decrease in the electron temperature to

172 the downward vertical transport process and the decrease in the cooling process to the upward vertical
173 transport process.

174

175 Figure 2 describes H , $B1$ and $B0$ in three columns respectively for all six stations. It was observed from the
176 plots that the minimum decrease in $NmF2$ amplitude corresponds to increase in H at all stations; implying
177 the upward lifting of the topside electron to the region of higher altitude at the eclipse window. Hence, the
178 scale height variation highlights the decrease in electron production and the vertical distance through
179 which the pressure gradient falls at the topside during the eclipse activity. The observation illustrates the
180 mutual relationship between the $NmF2$ and H , which may aid in extrapolating the topside ionospheric
181 profile (Gulyaeva, 2011). In essence, scale height changes observed during the eclipse window can be used
182 to explain the pressure gradient, electron density distribution and transport processes. In this sense, the
183 diffusion coefficients are expressed as ratio of determinants (determinant here refers to the concentration
184 of species ($[O]$ and $[N_2]$)), with the size of the determinants depending upon both the number of species in
185 the gas mixture and the level of approximation. Therefore, the increase (decrease) in the scale height can
186 be used as a proxy for downward (upward) diffusion process at the topside ionosphere. Consequently, the
187 thermospheric wind, which causes plasma distribution in the topside ionosphere, is induced by solar
188 radiation. Moreover, the significant changes observed in the scale height variation during the eclipse
189 window also indicated that transport processes are affected as they are temperature dependent.
190 Therefore, changes in the thermospheric compositions due to the solar eclipse at the topside layer will
191 affect the density profiles of the ionosphere (Müller-Wodarg et al., 1998).

192

193 It is noteworthy that the increase (decrease) in the scale height decreases (increases) the electron density
194 during the eclipse window. The sensitivity of electron density to temperature at the topside directly affects
195 the electron density profile (e.g. Wang et al., 2010); as cooling due to decrease in temperature results in
196 decrease in the electron density via reduced ionization. This indicates that the decrease (increase) in
197 electron temperature at the topside ionosphere causes the increase (decrease) in the scale height, which is
198 related to the diffusion and transport processes and subsequently affect the pressure gradient of the
199 plasma. From plots of H (fig. 2) and $NmF2$ (fig. 1), it was observed that the minimum decrease in $NmF2$
200 corresponded with peak increase in scale height. This imply that the topside ionosphere is more sensitive
201 (than the bottomside) to any change in the solar radiation. Thus, the pressure gradients can be analysed in
202 terms of either the scale height or electron density.

203

204 From column 2 and 3 of Figure 2, we observed that the measured shape ($B1$) and thickness ($B0$) parameters
205 of the ionosphere over these stations exhibit significant variations during the eclipse event. $B1$ responded

206 with a decrease at the first contact of the eclipse compared to the control day. This behaviour differs from
207 that of the *BO* observation. *BO* parameter from the first contact increases and reached the maximum peak
208 few minutes after the maximum obscuration magnitude, which coincided with the minimum decrease in
209 *BO*. Generally, the pattern of the day to day variation of the bottomside parameters is the average
210 morphology, but the increase in the *BO* and the decrease in the *B1* parameters during the eclipse period
211 compared to the control day was a notable one and can be related to the perturbation caused by the solar
212 eclipse. During the eclipse, the solar radiation was lost; trapped atomic ions O^+ was converted into
213 molecular ion (NO^+ and O_2^+) by charge transfer, owing to the sufficient concentration of molecular gasses
214 (N_2 and O_2) (Rishbeth, 1988). The height of the ionospheric slab indeed increased with reduced width,
215 which is attributable to compression due to loss of solar heating.

216

217 The behaviour of the ionosphere can be explained during solar eclipse with any of the components that
218 constitute the topside and the bottomside ionosphere and can be looked at, from the angle of the
219 percentage of concentration of the components. In this regard, the percentage of deviations of *NmF2*
220 (*DNmF2*) and *hmF2* (*DhmF2*) during the eclipse day away from the control day were plotted in Figure 3. This
221 is done to describe the contribution of the thermospheric wind and compositions. Although observing the
222 variation of *NmF2* and *hmF2* alone can be used for observing the changes in the behaviour of the
223 thermospheric compositions and wind flow, if properly analysed, but it is more convenient to describe
224 these mechanisms by standardizing the original variables used during the event. The normalization effort
225 (with the use of *DNmF2* and *DhmF2*) presents the original variation of *NmF2* and *hmF2* onto directions
226 which maximize the variance. Consequently, the result can be used for analyses of any mechanisms that
227 drive the ionospheric plasma, if properly related.

228

229 The percentage deviation in Figure 3 was defined as the ratio of $((NmF2e - NmF2c)/NmF2c) \times 100$. The
230 same relation is defined for the *hmF2* parameter. As earlier pointed out, during eclipse period, neutral
231 composition becomes the dominant chemical process arising from diffusion activities. The increase in the
232 neutral composition leads to the increase in the molecular gas concentration and compete with diffusion
233 process. Hence the percentage deviation in Fig. 3 discusses the neutral composition changes and delineate
234 how these changes may affect the electron densities as well as its profiles in the atmosphere during the
235 eclipse. The respective maximum and minimum peak response of the percentage deviation is attributed to
236 the enhancement and depletion of *DNmF2*. One sees from the plots that the percentage deviation started
237 increasing at the first contact of the eclipse (the dash vertical line) and reached the maximum, appearing
238 few minutes after the maximum magnitude of the eclipse was obtained. This behaviour is similar to the
239 conditions of the neutral compositions during the eclipse event reported by Muller-Wodarg et al. (1998).

240

241 Another important process observed in this study is the neutral wind flow effect. To identify the direction
242 of the wind, the $DNmF2$ colour legend in the contour plots was used in Figure 3. The negative values
243 represent a westward wind contribution and the positive values is for the eastward wind. Looking at the
244 marked eclipse region in the figure, it would be seen that the $DNmF2$ started decreasing from the first
245 contact of the eclipse and maximized few minutes after the totality mark and started increasing again. It
246 has been established that at daytime, the peak height of the plasma will be reduced due to lost in
247 recombination; but at nighttime, equatorward neutral wind drives the F2-layer plasma to higher altitudes
248 where ion loss rate is slower. The behaviour of the F2 plasma during solar eclipse cannot be completely
249 related to the nighttime period due to the fact that all the processes controlling the nighttime variation are
250 not completely actualised but can be related to partial nighttime/sunset period (see Adekoya et al., 2015).
251 Thus, the slight increase in the peak height and equatorward neutral wind flow is the driver during the solar
252 eclipse phase. The neutral wind acts jointly with the plasma flows from the topside ionosphere, resulting in
253 F2 region plasma density variation. Therefore, the westward/eastward neutral wind flow was related to the
254 depletion/enhancement in the deviation, which was clearly shown in the marked eclipse region of the
255 figure. The plot in Figure 3 had established the ionospheric dynamics of diffusion processes, neutral
256 compositions and the flow of neutral wind caused by the eclipse perturbation, which can invariably reduce
257 the effectiveness and reliability of radio wave propagation.

258

259 Relative to the mutual relationship between the topside and bottomside ionosphere, we considered the
260 linear correlation coefficient (R) of H versus $hmF2$ and H versus BO during the eclipse window, Figure 4. R
261 ranges from (0.52-0.92) for $H/hmF2$ relationship, and 0.37-0.92 for the H/BO connection. This good linear
262 agreement revealed the dependence of $hmF2$ and BO on the scale height. The only exception where low
263 correlation was observed was at Idaho (0.47) and Millstone (0.37) with respect to the H versus BO
264 relationship. Apart from revealing the dependence between the parameters, the relationship may also
265 provide a convenient way for modelling the topside profile from the knowledge of the bottomside
266 parameter, BO , during the eclipse period. Also, the strong correlation between $hmF2$ and H indicates that
267 there may be some inter-related physical mechanisms controlling the behaviour of the plasma at the
268 topside ionosphere. That is $hmF2$ strongly depend on the neutral wind flow and explain the state of
269 thermospheric composition (Liu et al., 2006; Fisher et al., 2015). Since all these parameters competes
270 during the eclipse, one can argue that with the accessibility of one, in place of the other (as a consequence
271 of their relationship), the prediction and modelling of the ionosphere can be conveniently achieved.

272

273 **4 Conclusions**

274 This paper presents the induced perturbation of solar eclipse of 21 August 2017 on the ionospheric F
275 parameters and how they describe the mechanisms of the ionosphere at mid-latitude. The perturbation
276 effects and dynamics during a solar eclipse episode using ionospheric F2 parameters (*NmF2* and *hmF2*), the
277 bottomside profile thickness (*B0*) and shape (*B1*) parameters of electron density and the plasma scale
278 height (H), which are not often used for eclipse study, were investigated. These parameters represent the
279 state of the F-region ionosphere. The changes observed during the eclipse phase is related to the reduction
280 in solar radiation and natural gas heating. The *NmF2* minimum was attained at ~30 minutes after the
281 totality of the eclipse when it decreases to about 65% of its control day. This decrease in *NmF2* was uplifted
282 to the higher altitude compared to the non-eclipse day. The thickness and shape parameters which are
283 often limited to the bottomside F-region were seen as viable parameters for probing the topside
284 ionosphere, relative to the scale height during the eclipse. Hence their relationship in describe one another
285 is established. Implication is that eclipse-caused perturbation could have been better explained using some
286 ionosonde parameters. The changes in the neutral wind flow, thermospheric compositions and diffusion
287 processes found their explanation in the behaviour of the F region plasma during eclipse. In addition, it can
288 be concluded that the behaviour of *DNmF2* and *DhmF2* during eclipse can be conveniently used to describe
289 the mechanisms of thermospheric composition and wind flow.

290

291 **Acknowledgements**

292 We acknowledge use of global ionospheric Radio Observatory data provided by ULMCAR
293 (<http://ulcar.uml.edu/DIDBase/>) and the World Data Center for Geomagnetism, Kyoto
294 (<http://wdc.kugi.kyoto-u.ac.jp/index.html>) for geomagnetic activity data. We thank the management team
295 of the national Aeronautics and Space Administration (NASA) service (<http://eclipse.gsfc.nasa.gov>) and
296 http://xjubier.free.fr/en/site_pages/SolarEclipseCalc_Diagram.html for progression and eclipse local
297 circumstances information. The authors thank Professor Ljiljana R, Cander and the anonymous reviewer for
298 their constructive corrections and suggestions that tremendously improved the structure and quality of the
299 paper.

300

301 **References**

302 Adeniyi, J. O., Radicella, S. M., Adimula, I. A., Willoughby, A. A., Oladipo, O. A., and Olawepo, O.: Signature
303 of the 29 March 2006 eclipse on the ionosphere over an equatorial station, *J. Geophys. Res.*, 112 (A6),
304 A06314. <http://dx.doi.org/10.1029/2006JA012197>, 2007.

305

306 Adekoya, B. J., Chukwuma, V. U., and Reinisch, B. W.: Ionospheric vertical plasma drift and electron density
307 response during total solar eclipses at equatorial/low latitude, *J. Geophys. Res.*, 120, 8066-8084.
308 doi:10.1002/2015JA021557, 2015.

309

310 Adekoya, B. J., and Chukwuma, V. U.: Ionospheric F2 layer responses to total solar eclipses at low- and mid-
311 latitude, *J. Atmos. Sol. Terr. Phys.*, 138-139, 136-160. <http://dx.doi.org/10.1016/j.jastp.2016.01.006>, 2016.

312

313 Belehaki, A., Marinov, P., Kutiev, I., Jakowski, N., and Stankov, S.: Comparison of the topside ionosphere
314 scale height determined by topside sounders model and bottomside digisonde profiles, *Adv. Space Res.*,
315 <http://dx.doi.org/10.1016/j.asr.2005.09.015>, 2006.

316

317 Cherniak, I., and Zakharenkova, I.: Ionospheric Total Electron Content response to the great American solar
318 eclipse of 21 August 2017, *Geophys. Res. Lett.*, <http://dx.doi.org/10.1002/2017GL075989> , 2018.

319

320 Chukwuma, V. U., and Adekoya, B. J.: The effects of March 20, 2015 solar eclipse on the F2 layer in the mid-
321 latitude, *Advances in Space Research*, 58, 1720-1731. <http://dx.doi.org/10.1016/j.asr.2016.06.038> , 2016.

322

323 Chuo, Y. J.: Ionospheric effects on the F region during the sunrise for the annular solar eclipse over Taiwan
324 on 21 May 2012, *Ann. Geophys.*, 31, 1891-1898. doi:10.5194/angeo-31-1891-2013, 2013

325

326 Fisher, D. J., Makela, J. J., Meriwether, J. W., Buriti, R. A., Benkhaldoun, Z., Kaab, M., and Lagheryeb, A.:
327 Climatologies of nighttime thermospheric winds and temperatures from Fabry-Perot interferometer
328 measurements: From solar minimum to solar maximum, *J. Geophys. Res.*, 120, 6679-6693,
329 doi:10.1002/2015JA021170, 2015.

330

331 Grigorenko, E. I., Lyashenko, M. V., and Chernogor, L. F.: Effects of the solar eclipse of March 29, 2006, in
332 the ionosphere and atmosphere, *Geomagnetism and Aeronomy*, 48 (3), 337-351.
333 <http://dx.doi.org/10.1134/S0016793208030092>, 2008.

334

335 Gulyaeva T. L.: Storm time behaviour of topside scale height inferred from the ionosphere-plasmasphere
336 model driven by the F2 layer peak and GPS-TEC observation, *Adv. Space Res.*, 47, 913-920.
337 doi:10.1016/j.asr.2010.10.025, 2011.

338

339 Hoque, M. M., Wenze, I. D., Jakowski, N., Gerzen, T., Berdermann, J., Wilken, V., Kriegel, M., Sato, H.,
340 Borries, C., and Minkwitz, D.: Ionospheric response over Europe during the solar eclipse of March 20, 2015,
341 *J. Space Weather Space Clim.*, 6 (A36). doi: 10.1051/swsc/2016032, 2016.

342

343 Huba, J. D., and Drob, D.: SAMI3 prediction of the impact of the 21 August 2017 total solar eclipse on the
344 ionosphere/plasmasphere system, *Geophys. Res. Lett.*, 44, 5928-5935.
345 <http://dx.doi.org/10.1002/2017GL073549>, 2017.

346

347 Huang, X. and B. W. Reinisch, B. W.: Vertical electron content from ionograms in real time, *Radio Sci.*, 36
348 (2), 335 – 342, 2001.

349

350 Jakowski, N., Stankov, S. M., Wilken, V., Borries, C., Altadill, D., Chum, J., Buresova, D., Boska, J., Sauli, P.,
351 Hruska, F. and Cander, Lj. R.: Ionospheric behaviour over Europe during the solar eclipse of 3 October 2005,
352 *J. Atmos. Sol. Terr. Phys.*, 70, 836-853. <http://dx.doi.org/10.1016/j.jastp.2007.02.016>, 2008.

353

354 Le, H., Liu, L., Yue, X., Wan, W., and Ning, B.: Latitudinal dependence of the ionospheric response to solar
355 eclipse, *J. Geophys. Res.*, 114, A07308. <http://dx.doi.org/10.1029/2009JA014072> , 2009.

356

357 Le, H. Le, Liu, Libo, Ding, Feng, Ren, Zhipeng, Chen, Yiding, Wan, Weixing, Ning, Baiqi, Guirong, Xu, Wang,
358 Min, Li, Guozhu, Xiong, Bo, Lianhuan, Hu: Observations and modeling of the ionospheric behaviors over the
359 east Asia zone during the 22 July 2009 solar eclipse. *J. Geophys. Res.*, 115, A10313.
360 <http://dx.doi.org/10.1029/2010JA015609>, 2010.

361

362 Liu, L., Wan, W., and Ning B.: A study of the ionogram derived effective scale height around the ionospheric
363 *hmF2*, Ann. Geophys., 24 (3), 851-860. www.ann-geophys.net/24/851/2006/, 2006.
364

365 Liu, L., Le, H., Wan, W., Sulzer, M. P., Lei, J., and Zhang, M. -L.: An analysis of the scale heights in the lower
366 topside ionosphere based on the Arecibo incoherent scatter radar measurements, J. Geophys. Res., 112,
367 A06307, <http://dx.doi.org/10.1029/2007JA012250>, 2007.
368

369 Müller-Wodarg, I. C. F., Aylward, A. D., and Lockwood, M.: Effects of a Mid-Latitude Solar Eclipse on the
370 Thermosphere and Ionosphere - A Modelling Study, Geophys. Res. Lett., 25(20), 3787-3790, 1998.
371

372 Reinisch, B. W., Dandenault, P. B., Galkin, I. A., Hamel, R., and Richards R. P.: Investigation of the electron
373 density variation during the August 21, 2017 Solar Eclipse, Geophys. Res. Lett., doi:
374 10.1002/2017GL076572, 2018.
375

376 Reinisch, B. W. and Galkin, I. A.: Global Ionosphere Radio Observatory (GIRO), Earth Planets Space, 63 (4),
377 377-381. <https://doi.org/10.5047/eps.2011.03.001>, 2011.
378

379 Reinisch, B. W., Huang, X., Belehaki, A., Shi, J., Zhang, M., and Ilma, R.: Modeling the IRI topside profile
380 using scale heights from ground-based ionosonde measurements, Adv. Space Res., 34 (9), 2026-2031.
381 <https://doi.org/10.1016/j.asr.2004.06.012>, 2004.
382

383 Reinisch, B. W., and Huang, X.: Deducing topside profiles and total electron content from bottomside
384 ionograms, Adv. Space Res., 27 (1), 23-30. [https://doi.org/10.1016/S0273-1177\(00\)00136-8](https://doi.org/10.1016/S0273-1177(00)00136-8), 2001.
385

386 Rishbeth, H.: Solar eclipses and ionospheric theory. Space Science Review, 8 (4), 543-554.
387 <https://doi.org/10.1007/BF00175006>, 1968.
388

389 Rishbeth, H.: Basic physics of the ionosphere: A tutorial review, Journal of Institute of The Electronics and
390 Radio Engineers, 58 (6S), S207-S223. doi:10.1049/jiere.1988.0060, 1988.
391

392 Xu, T. L., Jin, H. L., Xu, X., Guo, P. Wang, Y. B., Ping, J. S.: Statistical analysis of the ionospheric topside scale
393 height based on COSMIC RO measurements, J. Atmos. Sol. Terr. Phys., 104, 29 – 38.
394 <http://dx.doi.org/10.1016/j.jastp.2013.07.012>, 2013.
395

396 Wang, X., Berthelier, J. J., and Lebreton, J. P.: Ionosphere variations at 700 km altitude observed by the
397 DEMETER satellite during the 29 March 2006 solar eclipse, J. Geophys. Res., 115, A11312.
398 <http://dx.doi.org/10.1029/2010JA015497>, 2010.
399

400 Yonezawa, T.: Theory of formation of the ionosphere, Space Science Review, 5 (1), 3-56.
401 <https://doi.org/10.1007/BF00179214>, 1966
402

403
404
405
406
407
408
409
410

411 **Table Caption**

412 **Table 1:** List of ionosonde station, geographic coordinate, eclipse progression time and percentage of
413 maximum obscuration.

414

415

416 **Figure Captions**

417 **Figure 1:** Ionospheric $NmF2$ and $hmF2$ variations during the eclipse day (black continuous line) and the
418 control day (dash blue line). The three vertical lines represents the different phases of the eclipse (S - start
419 time of the initial phase, M - the period of the maximum magnitude of the eclipse, and E - the end time of
420 the recovery phase or the last contact of the eclipse progression).

421

422 **Figure 2:** The local time variation of the ionospheric scale height and the bottomside ($B0$ and $B1$). The other
423 features are the same as in Fig. 1.

424

425 **Figure 3:** Variation of the percentage deviation of $NmF2$ ($DNmF2$) and $hmF2$ ($DhmF2$) magnitudes for
426 observing the changes in the behaviour of the thermospheric composition and wind flow related to the loss
427 rate during the eclipse phase in comparing to the period before/after the event. The three vertical dashed
428 lines marked the eclipse start time, the time of maximum obscuration and the last contact time of the
429 eclipse (i.e. eclipse phase). The direction of wind was identify using the $DNmF2$ colour legend, the negative
430 values represents the westward wind direction and the positive values is for the eastward wind.

431

432

433

434

435

436

437

438

439

440

441

442

443

444

445

446

447

448

449

450

451

452

453

454
455
456
457
458
459
460
461

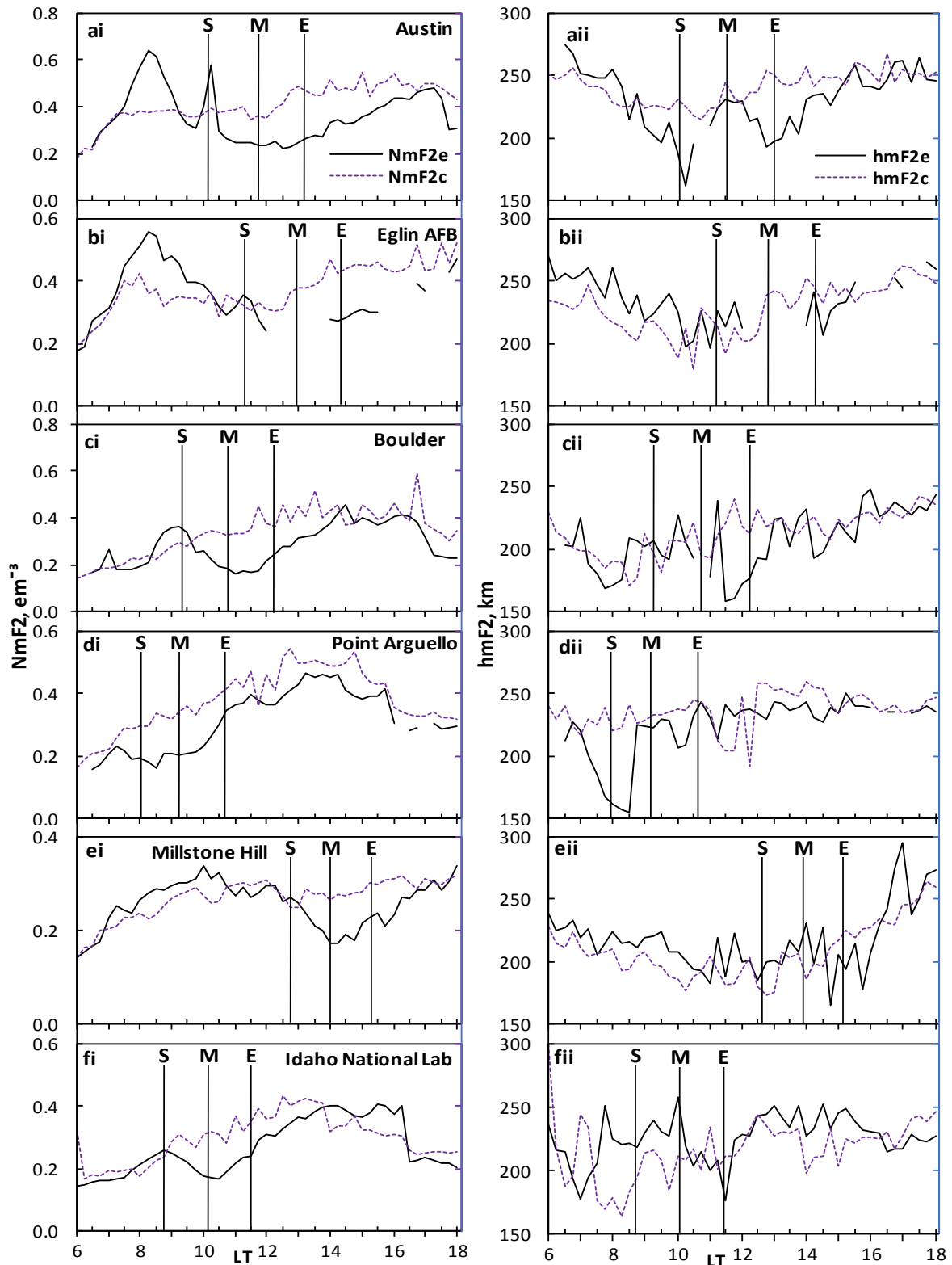
Table 1: List of ionosonde station, geographic coordinate, eclipse progression time and percentage of maximum obscuration.

| Station | GLat | GLong | Eclipse Start time (UT) | Eclipse Max Time (UT) | Eclipse End Time (UT) | % of max obscuration | UT to LT difference |
|--------------------|-------|--------|-------------------------|-----------------------|-----------------------|----------------------|---------------------|
| AUSTIN | 30.4 | 262.3 | 16:40:45.1 | 18:10:10.3 | 19:39:35.0 | 65.93 | 17:29.2 |
| EGLIN AFB | 30.5 | 273.5 | 17:04:41.1 | 18:37:07.6 | 20:03:47.7 | 83.322 | 18:13.8 |
| POINT ARGUELLO | 34.8 | 239.5 | 16:02:38.5 | 17:16:54.8 | 18:39:36.0 | 64.608 | 15:57.6 |
| BOULDER | 40 | 254.7 | 16:22:33.1 | 17:46:09.6 | 19:13:45.9 | 93.37 | 16:58.8 |
| MILLSTONE HILL | 42.6 | 288.5 | 17:27:28.1 | 18:45:52.5 | 19:58:38.3 | 62.533 | 19:13.8 |
| IDAHO NATIONAL LAB | 43.81 | 247.32 | 16:14:15.2 | 17:32:36.5 | 18:56:30.1 | 100 | 16:29.3 |

462

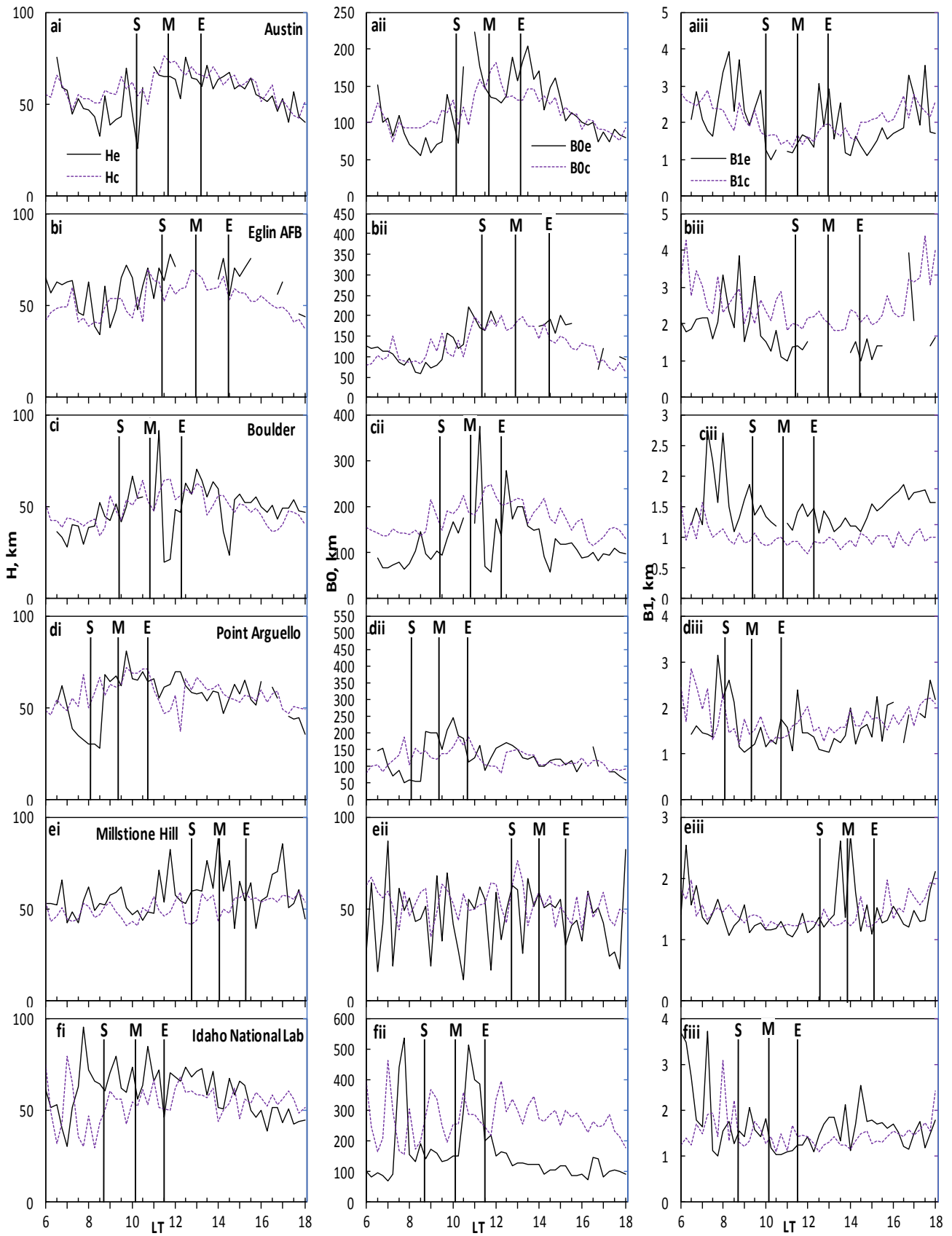
463
464

465



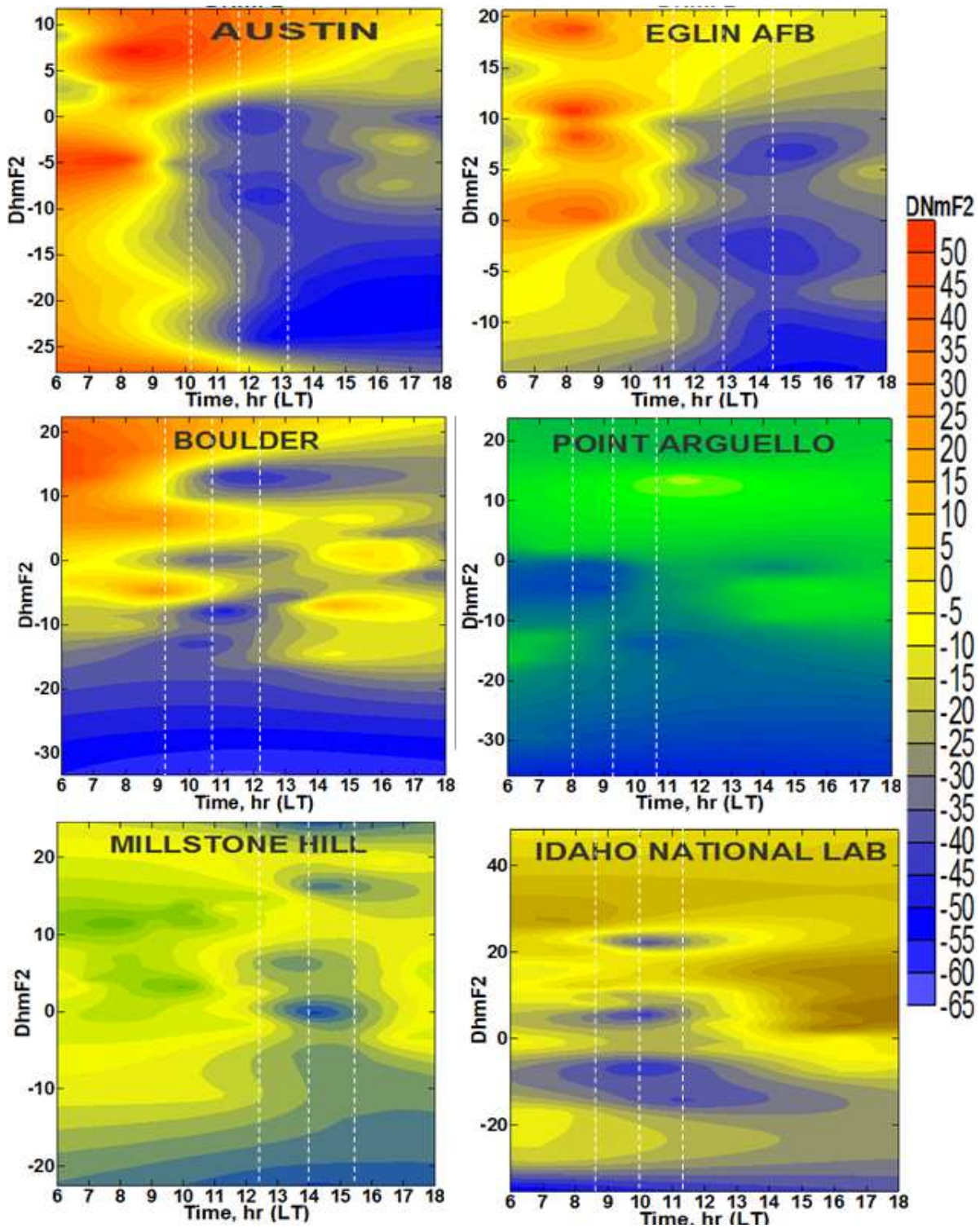
466

467 **Figure 1:** Ionospheric $NmF2$ and $hmF2$ variations during the eclipse day (black continuous line) and the
 468 control day (dash blue line). The three vertical lines represents the different phases of the eclipse (S - start
 469 time of the initial phase, M - the period of the maximum magnitude of the eclipse, and E - the end time of
 470 the recovery phase or the last contact of the eclipse progression).



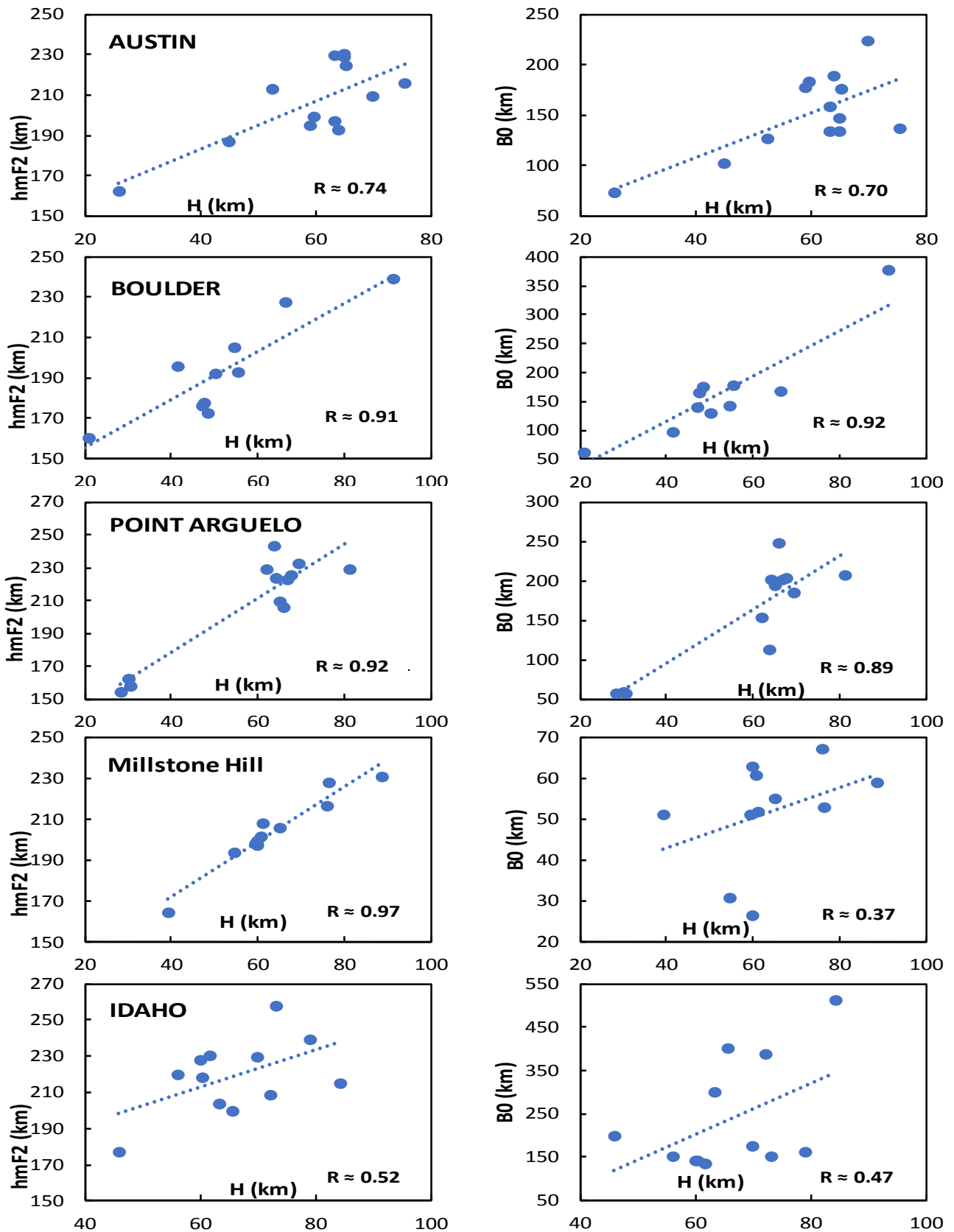
471

472 **Figure 2:** The local time variation of the ionospheric scale height and the bottomside ($B0$ and $B1$). The other
 473 features are the same as in Fig. 1.



474

475 **Figure 3:** Variation of the percentage deviation of $NmF2$ ($DNmF2$) and $hmF2$ ($DhmF2$) magnitudes for
 476 observing the changes in the behaviour of the thermospheric composition and wind flow related to the loss
 477 rate during the eclipse phase in comparing to the period before/after the event. The three vertical dashed
 478 lines marked the eclipse start time, the time of maximum obscuration and the last contact time of the
 479 eclipse (i.e. eclipse phase). The direction of wind was identify using the $DNmF2$ colour legend, the negative
 480 values represents the westward wind direction and the positive values is for the eastward wind.



481

482 **Figure 4:** Linear relationship of H versus *hmF2* and H versus *BO* during the eclipse of 21 August 2017
 483 progression phase.